



Fountain scheduling strategies for improving water-use efficiency of artificial ice reservoirs (Ice stupas)

Suryanarayanan Balasubramanian ^{a,b,*}, Martin Hoelzle ^a, Roger Waser ^c

^a University of Fribourg, Department of Geosciences, Fribourg, Switzerland

^b Himalayan Institute of Alternatives, Ladakh, India

^c University of Applied Sciences and Arts, Luzern, Switzerland

ARTICLE INFO

Keywords:

Ice stupa
Climate change adaptation
Nature-based solution
Water storage
Water resource management
Fountain engineering

ABSTRACT

Artificial ice reservoirs (AIRs), also called ice stupas, are a climate-change adaptation strategy developed in the Indian Himalayas (Ladakh). With this technology, otherwise unused stream/spring water is stored in large ice towers during the winter. The surplus melt water generated in spring is used to satisfy irrigation water demands. Recent studies have shown that, during AIR construction, over 75% of the water sprayed is lost. In order to reduce these water losses, different fountain scheduling strategies implemented on two AIRs under identical weather conditions were compared. In one scheduling strategy, the fountain was operated manually (non-scheduled fountain) whereas in another it was operated via an automation system (scheduled fountain). The automation system computed recommended discharge rates using real-time meteorological input and location metadata. Scheduled fountains produced similar ice volume while consuming one-tenth of the water the non-scheduled fountain used. Simulations converting non-scheduled fountains into scheduled fountains showed a threefold improvement in water-use efficiency. Overall, these results show that automated fountain water supply management can increase water-use efficiency of AIRs and reduce their maintenance without compromising their meltwater production.

1. Introduction

Climate warming has resulted in retreat and thinning of mountain glaciers (IPCC, 2022). This has implications for water availability in river basins that have considerable glacierized areas in their headwaters, such as High Mountain Asia (HMA). Glaciers in HMA provide an important gradual release of water that is used by many people locally and downstream for irrigation, drinking water and hydropower. Climate change in this densely populated region may have serious consequences for glacier melt water supply to the rivers (Immerzeel et al., 2020). In this context, the development of water storage technologies is crucial to ensure continued sustenance of cryosphere-fed irrigation networks.

These issues are particularly pronounced in arid and semiarid regions, where it is estimated that between 50% and 90% of freshwater resources originate from mountain catchments (Mukhopadhyay and Khan, 2015). Especially in the cold-arid Trans-Himalayan region of Ladakh, meltwater supply from the cryosphere is of utmost importance for irrigated agriculture in spring and summer, when water demand is highest. Due to the short growing period, central Ladakh is a single-

cropping area with barley and wheat as important staples, complemented by vegetables, pulses, and oil seeds. Depending on the altitude, irrigation with complete flooding of fields starts between March and April prior to the melting of high-altitude glaciers. This results in increased demand during a period of reduced supply at the onset of the agricultural season (Nüsser et al., 2019a, 2019b).

To cope with this recurrent water scarcity, villagers have developed artificial ice reservoirs (AIRs; Fig. 1a). AIRs capture water during autumn and winter, freezing and holding it until spring, when this water melts and flows down to irrigate the fields (IPCC, 2019; Vince, 2009; Clouse et al., 2017; Nüsser et al., 2019a); thus retaining a previously unused portion of the annual flow and facilitating its use to compensate the decreased flow during the following spring. Over the past decade, several AIRs have been built to supplement the irrigation water supply of mountain villages in India (Wangchuk, 2020; Palmer, 2022; Aggarwal et al., 2021), Pakistan (Awaz Production, 2022), Kyrgyzstan (BBC News, 2020), Nepal, and Chile (Reuters, 2021). In total, more than 500 farmers have constructed AIRs across 30 villages in the Alps, Andes and HMA.

A spirit of improvisation guides the construction strategy of AIRs,

* Corresponding author at: University of Fribourg, Department of Geosciences, Fribourg, Switzerland.

E-mail address: suryanarayanan.balasubramanian@unifr.ch (S. Balasubramanian).

challenging their classification. Construction strategies using fountain systems form AIRs which tend towards a conical shape, whereas other strategies form flat sheets of ice. Therefore, in the present study, the AIRs are classified based on whether or not fountain systems are used for their construction. AIRs using fountain systems are called ice stupas (Fig. 1c) and those without are called ice terraces (Fig. 1b). In the present work, the ice stupa form of AIRs are investigated.

A common issue of AIR construction systems is fountain scheduling, namely answering the questions “when to spray?,” “how much?,” and “for how long?.” Starting a fountain spray too early, spraying too much water, or running a fountain spray for too long might lead to overwatering; at the very least, this practice wastes water. Similarly, starting the fountain spray too late, spraying too little water, or not running the system for long enough might lead to underwatering and can cause reduced ice volume or freeze the water supply pipelines. Previous work (Balasubramanian et al., 2022) has shown that manual construction systems suffer from overwatering. To avoid this issue, the energy balance model developed in Balasubramanian et al. (2022) can be used to regulate fountain water supply through its surface freezing rate estimations. Recommended discharge rates can be produced from such estimations if uncertainties of the fountain, meteorological and surface characteristics are resolved. However, some of these properties like fountain spray radius, cloudiness, albedo and AIR slope cannot be predicted beforehand. Additionally, discharge rates recommended need to be sensitive to constraints on water supply or weather conditions at the construction site; for example, locations limited by their water supply such as Ladakh, India would prioritize water-use efficiency, whereas those limited by the duration of their favorable weather windows such as Guttannen, Switzerland would prioritize maximum ice volume. Therefore, the upper and lower bound of each uncertain variable/parameter can be associated with two model types depending on their influence on the freezing rate estimation. The model type that overestimates freezing rates can be used to regulate fountains in locations that want higher ice volumes and the other model type can be used to

regulate fountains in locations that want higher water-use efficiency.

Other practical issues need to be addressed along with fountain scheduling processes: for example, in Indian AIRs, the fountain discharge rate could theoretically be halved since this is always twice as high as the modelled freezing rate (Balasubramanian et al., 2022). However, in practice, a reduction of the discharge rate could increase the maintenance cost due to a higher risk of freezing events in the fountain pipeline. Therefore, an optimum fountain operation strategy should prevent the occurrence of any freezing events by setting a minimum threshold for the recommended discharge rate.

Adjusting fountain discharge rates in response to significant diurnal and seasonal variations of freezing rates requires the use of automation systems. Therefore, this paper describes such an automated construction strategy that can reduce water losses and maintenance requirements compared to manual construction strategies. First, two AIRs were built in the same location with and without automated fountain scheduling strategies; both were measured and compared. In a second step, differences in construction strategies between Indian and Swiss AIRs studied in previous winters were quantified using model simulations.

2. Site locations and data collection

In the present work, data sets from Balasubramanian et al. (2022) are used along with new data sets. These old data sets record the meteorological conditions and fountain characteristics of AIRs built in Gangles, India (IN21) and Guttannen, Switzerland (CH21) during the winter of 2020–21. The new AIR data sets were collected in Guttannen, Switzerland during the winter of 2021–22 (CH22).

The Guttannen site (46.66°N , 8.29°E) is situated in the Berne region, Switzerland at an altitude of 1047 m a.s.l. During the winter (Oct-Apr), mean daily minimum and maximum air temperatures vary between -13 and 15 °C. Clear skies are rare, averaging around 7 days during winter. Daily winter precipitation can sometimes be as high as 100 mm. These values are based on 30 years of hourly historical weather data

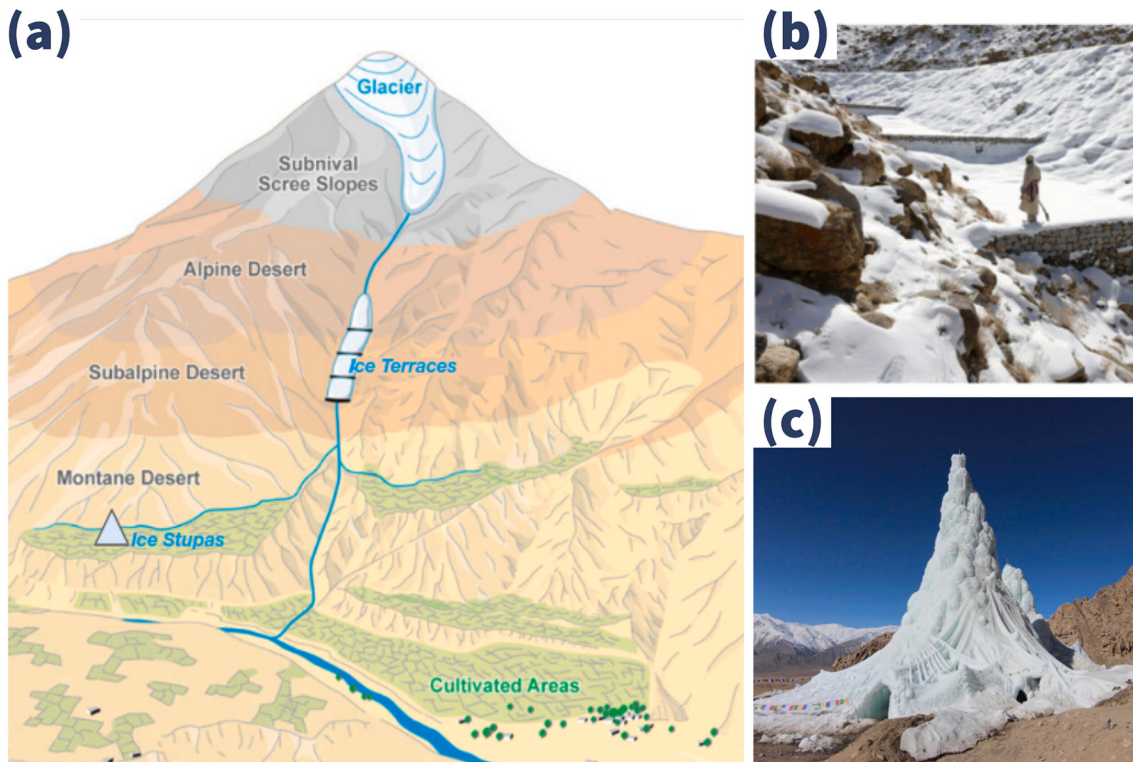


Fig. 1. (a) Schematic overview of artificial ice reservoirs (AIRs) located at altitudes between the glaciers and the irrigation networks in the cultivated areas; (b) ice terraces and (c) ice stupas are located at higher and lower altitudes, respectively. Adapted from: Nüsser and Baghel (2016).

measurements (Meteoblue, 2021). Two AIRs were constructed by the Guttannen Bewegt Association, the University of Fribourg, and the Lucerne University of Applied Sciences and Arts during the winter of 2021–22 using a manual and an automated construction strategy.

The automated and manual AIRs were constructed adjacent to each other with different fountain designs, as shown in Fig. 2. This ensures both AIRs share water source and identical weather conditions. In addition, a webcam guaranteed continuous surveillance of the automated AIR.

In the AIR constructed with the manual strategy, tree branches were laid covering the fountain pipe to initiate and accelerate the ice cone formation process. In the AIR constructed with an automated strategy, only the fountain pipe was placed before the water spray started. Construction of both AIRs began on December 8, 2021 (start date) on a 0.1-m-thick snow bed and ended on April 12, 2022 (expiry date).

In the manual AIR, the fountain was always operated at maximum possible discharge rate, whereas in the automated AIR, the fountain discharge rate was controlled using real-time weather input and several control parameters which could be modified via a user interface (Fig. 3). Henceforth, the fountain used in the manual AIR is referred as non-scheduled fountain and the fountain used in the automated AIR is referred as scheduled fountain.

2.1. Meteorological data

To calculate the surface energy balance of an AIR, the following variables are required: air temperature, relative humidity, wind speed, pressure, precipitation, incoming longwave radiation, shortwave radiation, and cloudiness index. The primary weather data source is an automatic weather station (AWS) located within 20 m from the AIRs. It measured all the required variables except precipitation and cloudiness index at an hourly resolution from November 30 to April 12, 2022. Additionally, ground temperature measurements at a depth of 0.3 m were also recorded by the AWS to obtain approximate values of the fountain water temperature. Less than 0.4% of data was missing, and data gaps were filled by linear interpolation. The cloudiness index and

precipitation variables were obtained from ERA5 reanalysis dataset (Hersbach et al., 2020) and a MeteoSwiss AWS located 184 m from the AIRs (Station ID: 0-0756-0-GTT), respectively.

2.2. Fountain pipeline observations

Figure 3 presents all the attributes of the scheduled fountain pipeline system. Discharge rate (Q) represents the discharge rate of water measured by the flowmeter. Fountain height (h_f) denotes the height of the fountain pole. Fountain water temperature (T_f) is the temperature of water droplets produced by the fountain. Source water pressure (P_{source}) is the pressure of water measured at the pipeline input. Pipeline length and diameter (L_p , dia_p) denotes the dimensions of the pipeline used. P_{alt} is the pressure loss due to the altitudinal difference between the pipeline input and fountain output. The frictional pressure losses of the pipeline are denoted by $P_{friction}$. The nozzle pressure loss (P_f) denotes the pressure consumed during the formation of water droplets. The nozzle diameter (dia_f) denotes the size of the aperture through which water droplets are ejected. Spray radius (r_f) denotes the radius formed by the fountain water droplets.

Height was increased in steps of 1 m for both fountains. For the scheduled fountain, the initial height was 3 m and was increased to 4 m on December 23. For the non-scheduled fountain, the initial height was 3.7 m and was increased twice—December 23 and February 12.

Figure 4 shows the temporal variation in temperature and discharge rate for both the scheduled and non-scheduled fountains. The non-scheduled fountain showed variations in discharge rate whenever the fountain height was increased. The discharge rate variations of the scheduled fountain were caused by the ball valve of the automation system (Fig. 3). The ball valve position between 0 and 100% (or 0 to 90°) was regulated by the control box using real-time meteorological conditions measured by the AWS. Throughout the study period, the ball valve was opened completely (100%) only once, corresponding to the moment in time when temperature attained its minimum of -13°C on December 20. The ball valve was never opened beyond 34% thereafter.

The non-scheduled fountain was manually operated to spray all the



Fig. 2. Non-scheduled and scheduled fountains used for construction of manual and automated AIRs at Guttannen. Photo: Daniel Bürki.

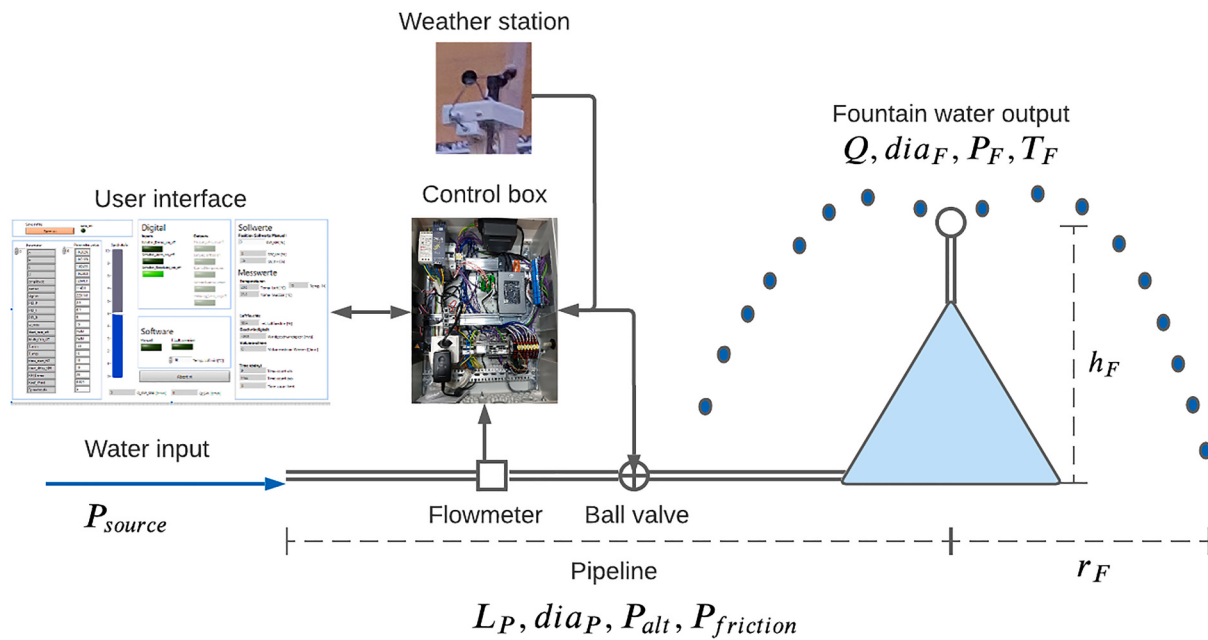


Fig. 3. Schematic illustrating the measurement and control of the fountain pipeline system through the automation system. Two-way arrows indicate information exchange between different components whereas one-way arrows indicate information transmission. Q represents the discharge rate of water measured by the flowmeter. h_F denotes the height of the fountain. T_F is the temperature of water droplets produced by the fountain. P_{source} is the pressure of water measured at the pipeline input. L_P , dia_P denotes the length and diameter of the pipeline used. The altitudinal and frictional pressure losses of the pipeline are denoted by P_{alt} and $P_{friction}$ respectively. P_F denotes the pressure consumed during the formation of water droplets. dia_F denotes the diameter of the aperture through which water droplets are ejected. r_F denotes the spray radius formed by the fountain water droplets.

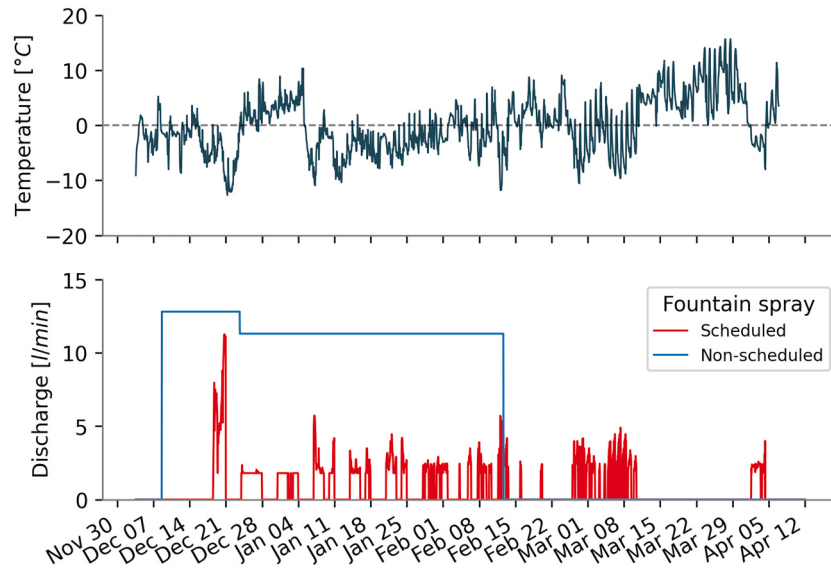


Fig. 4. Temperature and discharge measurements of the two fountains at the Guttannen construction site.

available discharge until a fountain freezing event interrupted the discharge on February 17. Unfortunately, no discharge rate measurements were recorded for the non-scheduled fountain. However, the non-scheduled fountain presented a higher discharge rate compared with the scheduled fountain due to its higher aperture diameter (Fig. 2). Therefore, we conservatively assume the discharge rate of the non-scheduled fountain to be equal to the maximum discharge rate of the scheduled fountain, which was observed to be 13 l/min and 11 l/min at a fountain height of 3 m and 4 m, respectively.

2.3. Drone surveys

Several photogrammetric surveys were conducted on the manual and the automated AIRs. The digital elevation models (DEMs) generated from the obtained imagery were analysed to document ice radius, surface area, and volume of the ice structures. Ice radius measurements from drone flights showed either an increase in AIR circumference or volume and were averaged to determine the fountain spray radius. The number of drone surveys conducted for the manual and the automated AIRs was 8 and 6, respectively (Table 1). We attach a high uncertainty of $\pm 10\%$ for all AIR observations to accommodate for the uncertainties in

Table 1
Summary of drone surveys.

	No.	Date	Volume	Radius	Surface area
Manual	1	Dec 23, 2021	17 m ³	2.9 m	47 m ²
	2	Jan 3, 2022	22 m ³	3.4 m	61 m ²
	3	Jan 22, 2022	35 m ³	4 m	79 m ²
	4	Feb 6, 2022	44 m ³	4.2 m	86 m ²
	5	Feb 20, 2022	43 m ³	4.3 m	86 m ²
	6	Mar 19, 2022	33 m ³	4.4 m	84 m ²
	7	Mar 26, 2022	24 m ³	4.3 m	74 m ²
	8	Apr 12, 2022	11 m ³	3.5 m	50 m ²
Automated	1	Dec 23, 2021	35 m ³	4.3 m	73 m ²
	2	Jan 3, 2022	32 m ³	4.4 m	81 m ²
	3	Feb 20, 2022	60 m ³	5.3 m	105 m ²
	4	Mar 19, 2022	28 m ³	3.7 m	57 m ²
	5	Mar 26, 2022	19 m ³	3.7 m	53 m ²
	6	Apr 12, 2022	7 m ³	2.5 m	53 m ²

the geodetic processing methodology described in the supplementary materials of [Balasubramanian et al. \(2022\)](#).

3. Methods

3.1. Fountain scheduling software

Recommended discharge rates can be produced only when information about AIR surface properties and weather conditions is available. In particular, resolving the uncertainty in the expected freezing rate requires quantification of slope, albedo, and cloudiness. However, these properties cannot be predicted, and therefore, the upper and lower bound of each variable is associated with a different model depending on whether these increase the freezing rate or not. The equations quantifying the influence of albedo, slope and cloudiness on all the energy fluxes are provided in Appendix A. Higher albedo and slope values decrease the net shortwave radiation impact. Higher cloudiness values increase both the net shortwave and the longwave radiation impact. The model overestimating the freezing rate is hereinafter referred as ice volume optimized model (IVOM) and the model underestimating the freezing rate, water-use efficiency optimized model (WEOM). Accordingly, the values assigned for all three variables in each model are presented in [Table 2](#).

The discharge scheduling software implements two types of fountain scheduling strategies depending on which model type is suitable. The WEOM model type is used when the location presents limited water quantity, as this is expected to produce better water-use efficiency. The IVOM model type is used when the location presents limited duration of favorable weather windows, as this is expected to produce higher ice volume. These two types of scheduled fountains are hereafter referred as water-sensitive fountain and weather-sensitive fountain, respectively.

The assumptions described in [Table 2](#) are applied on the one-dimensional description of energy fluxes as used in [Balasubramanian et al. \(2022\)](#) to obtain the rate of change of AIR ice mass as follows:

$$\frac{\Delta M_{ice}}{\Delta t} = \left(\frac{q_{SW} + q_{LW} + q_S + q_F + q_R + q_G - q_T}{L_F} + \frac{q_L}{L_V} \right) \cdot A_{cone} \quad (1)$$

Upward and downward fluxes relative to the ice surface are positive and negative, respectively. The first term represents the mass change

Table 2

Assumptions for the parametrization introduced to simplify the ice volume optimized model (IVOM) and the water-use efficiency optimized model (WEOM). $\alpha_{snow/ice}$ represents albedo of snow or ice.

Estimation of	Symbol	IVOM	WEOM
Slope	s_{cone}	1	0
Albedo	α	α_{snow}	α_{ice}
Cloudiness	cld	0	1

rate due to freezing of the fountain water and melting of the ice. q_{SW} is the net shortwave radiation; q_{LW} is the net longwave radiation; q_L and q_S are the turbulent latent and sensible heat fluxes, respectively; q_F is the fountain discharge heat flux; q_R is the rain water heat flux; q_G is the bulk heat flux between the AIR surface and its interior; q_T is the heat flux accounting for surface temperature fluctuations, and A_{cone} is the area of the AIR surface. L_F and L_V represent latent heat of fusion and vaporization, respectively. The derivation of these individual terms for the IVOM and WEOM model versions are discussed in Appendix A.

Eq. 1 is implemented in the automation software. The user interface of the software enables input of the spray radius, altitude, latitude, and longitude of the construction location. The automation hardware consists of an AWS, control box, flowmeter, ball valve, drain valves, air valves, fountain and a pipeline ([Fig. 3](#)). The control box feeds the AWS data to the automation software to obtain the recommended discharge rate. Then, to match this recommendation, it adjusts the ball valve position based on the information from the flowmeter. In case a termination criterion gets met, the drain and air valves are opened to allow removal of water and entry of air in the pipeline, respectively.

The recommended discharge rate is equal to the mass change rate. However, these termination criteria override the discharge rate recommendation and drain the pipeline to prevent water loss or fountain freezing events:

- High water loss is assumed when wind speed is greater than user-defined critical wind speed.
- High risk of fountain freezing is assumed when mass change rate is lower than user-defined minimum fountain discharge rate.
- Freezing events in fountain pipeline are assumed when measured discharge rate equals zero for at least 20 s.
- Pipeline leakage is assumed when measured discharge rate is greater than user-defined maximum fountain discharge rate.

3.2. Modelling fountain spray radius

Fountain spray radius is defined as the largest horizontal distance covered by fountain water droplets. This can be determined by modelling the trajectory of these droplets using the projectile motion equation. This projectile motion starts at the fountain nozzle and ends at the AIR surface. To obtain the droplets speed (v), the measured aperture diameter ($dia = 0.001\text{m}$) and discharge rate of the scheduled fountain is used with the following equation:

$$v = \frac{4 \cdot Q}{60 \cdot 1000 \cdot \pi \cdot dia^2} \quad (2)$$

where v is the droplet speed in m/s and Q is the discharge rate of the fountain in l/min .

To obtain the spray radius (r_F), the optimum launch angle $\theta = 45^\circ$ is used in the projectile motion equation to get:

$$r_F = \frac{v \cdot (v + \sqrt{v^2 + 4hg})}{2g} \quad (3)$$

The influence of wind-driven redistribution can be included in the spray radius by multiplying wind speed by time of flight of water droplets.

3.3. Determination of pressure losses

The fountain pipeline system delivering water to the ice stupa suffers several pressure losses, which limit the maximum height that the fountain can achieve. These losses can be (a) altitudinal (P_{alt}), (b) frictional ($P_{friction}$), and (c) nozzle (P_F) losses as illustrated in [Fig. 3](#). The altitudinal losses depend on the altitude difference between the source and the fountain. The frictional losses are proportional to the length of the pipeline and inversely proportional to their diameter. The nozzle

losses depend on the engineering design of the fountain nozzle. All the pressure variables are measured in bars.

Pressure losses can be determined using the Bernoulli equation as follows:

$$P_{\text{source}} = P_{\text{alt}} + P_{\text{friction}} + P_F + \frac{\rho \cdot v^2}{2} \cdot 10^{-5} \quad (4)$$

The frictional loss of the pipeline used in the experiment can be determined using the Hagen–Poiseuille equation (Batchelor, 2000):

$$P_{\text{friction}} = \frac{3.2 \cdot \mu \cdot v \cdot L_p}{\rho \cdot g \cdot dia_p^2} \quad (5)$$

where L_p is measured in meters. Note that the above equation only applies for laminar flow, the one investigated in the present work.

3.4. Model updates

The present study focuses on the integration of fountain scheduling processes with the AIR model (Balasubramanian et al., 2022). For details on model internals and calculation of surface processes, please refer to the respective literature references.

In the previous version of the model (Balasubramanian et al., 2022), fountain water droplet temperature (T_F) was estimated as a constant parameter. However, in reality, this is a poor approximation because it does not account for two processes, namely temperature fluctuations during transit from the source to the fountain nozzle or temperature fluctuations during the flight time of water droplets after leaving the fountain nozzle. Therefore, the first process is approximated with hourly ground temperature values. To approximate the second process, the water temperature is assumed to cool down to 0 °C during subzero air temperature conditions.

In the previous version of the model (Balasubramanian et al., 2022), fountain discharge events were reset from surface albedo to ice albedo. However, this assumption limits the accuracy of the model, especially for the automated AIR, where several fountain discharge events of short duration occur. Therefore, the discharge events are assumed to reduce the albedo decay rate (τ) by a factor of $\frac{\alpha_{\text{ice}}}{\alpha_{\text{snow}}}$.

Additionally, both AIRs experienced numerous precipitation events. Therefore, instead of assuming AIR density (ρ_{cone}) to be equal to ice density—which was no longer accurate—the density parametrization was changed as follows:

$$\rho_{\text{cone}} = \frac{M_F + M_{\text{dep}} + M_{\text{ppt}}}{(M_F + M_{\text{dep}})/\rho_{\text{ice}} + M_{\text{ppt}}/\rho_{\text{snow}}} \quad (6)$$

where M_F is the cumulative mass of the fountain discharge, M_{ppt} is the cumulative precipitation, M_{dep} is the cumulative accumulation through water vapour deposition, ρ_{ice} is the ice density (917 kg m^{-3}), and ρ_{snow} is the density of wet snow (300 kg m^{-3}) taken from Cuffey and Paterson (2010).

Rain events were not considered in the previous version of the model, but these occurred in this experiment. The influence of rain events on the albedo and the energy balance was assumed to be similar to the discharge events. However, the water temperature of a rain event was assumed to be equal to the air temperature; accordingly, the rain water heat flux (q_R) generated due to a rain event was equal to:

$$q_R = \frac{\Delta M_{\text{ppt}} \cdot c_{\text{water}} \cdot T_a}{\Delta t \cdot A_{\text{cone}}} \quad (7)$$

where M_{ppt} is the hourly precipitation in meters, c_{water} is the specific heat of water, and A_{cone} is the surface area.

3.5. Calibration

The model parameters were calibrated to the mean values of the

ranges presented in Appendix Table A1. However, the surface layer thickness parameter was calibrated to a value of 0.09 m for the automated AIR instead of the default value of 0.05 m. This calibration was necessary to prevent hourly surface temperature fluctuations from assuming unphysical values above 40 °C.

The validation of the model for the manual and automated AIRs were evaluated using the root mean squared error (RMSE) between volume estimates and measurements.

Performance of the IVOM and WEOM versions of the physical model were assessed by comparing the correlation of its discharge rate estimates with the validated freezing rates of the manual AIR.

4. Results

4.1. Model validation

The volume estimation for the automated and manual AIRs showed an RMSE of 8 m^3 and 6 m^3 , respectively, with the drone volume observations. These are within 13% and 11% of the maximum volume of the automated and the manual AIR, respectively. The estimated and measured AIR volumes are shown in Fig. 5.

4.2. Comparison of AIR construction strategies

Table 3 presents the influence of the two different fountain scheduling strategies in the mass and energy balance of their respective AIRs. The overall impact of the radiation fluxes—longwave and shortwave—and the turbulent fluxes—sensible and latent—on the freezing and melting energies is determined by their energy turnover, which is calculated as the sum of energy fluxes in absolute values (Table 3).

Fountain scheduling reduced the fountain discharge input and fountain spillwater output by an order of magnitude. However, this does not result in an appreciable difference in the volume evolution of the automated or manual AIR, as shown in Fig. 5. This is due to two counteracting surface processes during fountain spray: process A consists in the dampening of albedo to ice albedo and process B consists in the absorption of heat energy from the fountain water droplets. The temporal variation of the magnitude of these processes is shown in Fig. 6.

A considerable difference exists in the contribution of the shortwave radiation due to process A. Although the non-scheduled fountain was active for a longer duration, frequent snowfall events counteracted the albedo feedback of the fountain discharge. In contrast, the albedo of the automated AIR was reduced by late fountain spray events, in particular in March and April, as shown in Fig. 6. These poorly timed fountain spray events occurred because of the global solar radiation diurnal

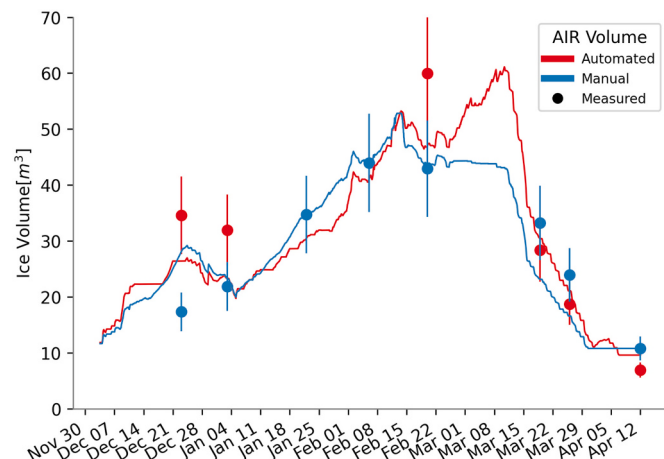


Fig. 5. Volume validation of the scheduled and non-scheduled fountain construction strategies.

Table 3

Summary of the mass balance, energy balance, and fountain and AIR characteristics estimated at the end of the respective simulation duration for the automated and the manual AIRs.

	Name	Symbol	Manual	Automated	Units
Input	Fountain discharge	M_F	1.1×10^6	1.5×10^5	kg
	Snowfall	M_{Ppt}	9.2×10^3	1.4×10^4	kg
	Deposition	M_{dep}	4.0×10^2	4.5×10^2	kg
Output	Meltwater	M_{water}	4.5×10^4	5.4×10^4	kg
	Ice	M_{ice}	7.4×10^3	6.1×10^3	kg
	Sublimation	M_{sub}	3.7×10^3	4.5×10^3	kg
Energy flux	Fountain spillwater	M_{waste}	1.07×10^6	1.0×10^5	kg
	Shortwave radiation	q_{SW}	14	21	%
	Longwave radiation	q_{LW}	25	25	%
AIR	Sensible heat	q_s	38	33	%
	Latent heat	q_L	19	19	%
	Maximum AIR volume		53	61	m^3
	Water-use efficiency		4	35	%

variation, since these were calibrated based on values for February in the automation system. Therefore, poor calibration of the automation system resulted in an increased impact of shortwave radiation on the automated AIR. Similarly, the fountain discharge heat flux for the manual AIR was enhanced due to process B. The higher discharge value of the non-scheduled fountain and its longer duration are responsible for the higher contribution of fountain discharge heat flux in the overall energy turnover. Therefore, higher melt of the automated AIR due to process A counteracted the higher melt of the manual AIR due to process B.

4.3. Benefits of scheduling fountains

The difference in water-use efficiency and maximum ice volume between non-scheduled and scheduled fountains in the Indian and Swiss locations across two winters is shown in Fig. 7a. Four experimental values (highlighted in circles) and five simulated values (highlighted in squares) are shown together. The experimental values were taken from the IN21 and CH21 AIRs studied in Balasubramanian et al. (2022) and

the CH22 AIR investigated in the present work.

The water-use efficiency of all the non-scheduled fountains is below 20%. In general, water-use efficiency exhibits a threefold increase when the weather- or water-sensitive fountains are used in both locations.

For the Indian location, the three different kinds of fountains yielded significantly different results owing to discharge duration and maximum discharge rate (Fig. 7b). The non-scheduled fountain showed a maximum discharge rate more than twice that of the scheduled fountains, resulting in higher water loss; freezing events in its pipeline caused frequent interruptions in the non-scheduled discharge rate (Fig. 7b). In contrast, the mean freezing rates of the other two fountains during these events were above their median values. This is because very cold temperatures freeze the water inside rather than outside the fountain system, instigating these freezing events in the fountain pipeline. Therefore, the discharge duration of the non-scheduled fountain was much lower, resulting in lower ice volume. The water-sensitive fountain underestimated the freezing rate during the construction period and therefore produced much lower ice volume compared with the weather-sensitive fountain.

For the Swiss locations, scheduled fountains yielded better water-use efficiency but did not significantly alter the maximum volume obtained. The maximum volume and the water-use efficiency of the scheduled fountain used in the CH22 experiment was similar but not equal to the simulated values produced from the IVOM model (Fig. 7a). This was because the IVOM model was approximated with linear and gaussian equations due to the limitations of the fountain scheduling software implemented in the automation system.

4.4. Performance of weather- and water-sensitive fountains

The WEOM and IVOM model versions estimated the freezing rate of the non-scheduled fountain with an RMSE less than $0.8 l/min$ and $1.8 l/min$, respectively, and a correlation of 0.4. The discharge rate values of the weather-sensitive fountain overestimated the freezing rate 93% of the fountain spray duration, whereas those of the water-sensitive fountain overestimated the freezing rate 70% of the non-scheduled fountain spray duration, as illustrated by Fig. 8. Therefore, the IVOM model version was successful in prioritizing the maximum ice volume by overestimating the discharge rates, but the WEOM model version could not sufficiently underestimate its discharge rate values to optimize water-use efficiency.

However, for the Indian location, considerable differences can be

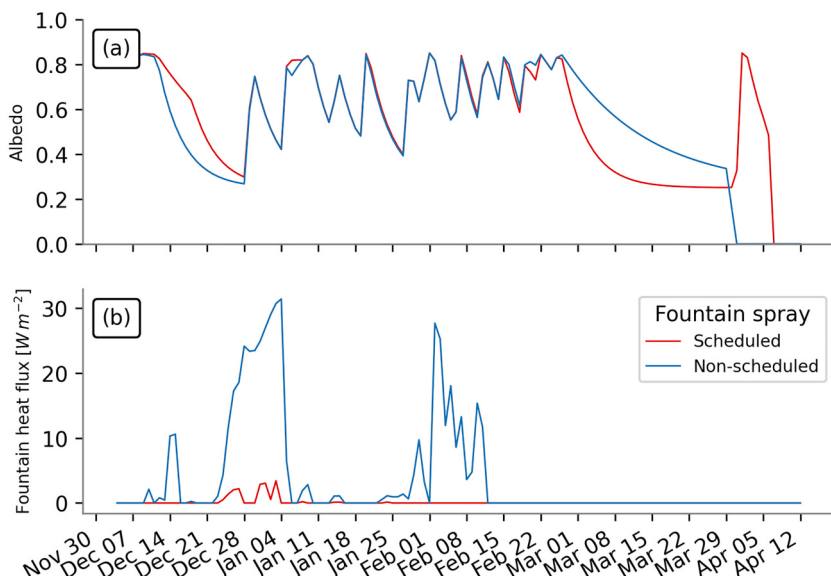


Fig. 6. (a) Surface albedo and (b) fountain discharge heat flux (q_F) showed considerable variations between the two AIRs due to differences in their discharge rates.

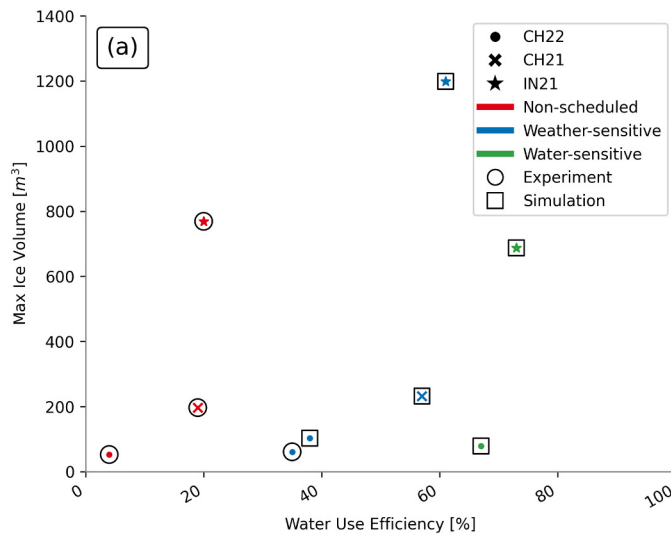


Fig. 7. (a) The maximum volume and water-use efficiency estimated for AIRs constructed in different locations (represented by symbols) with different fountain scheduling strategies (represented by colours). Experimental values are highlighted in circles and simulated values are highlighted in squares. (b) Comparison of the non-scheduled and scheduled fountain discharge rates at the IN21 location.

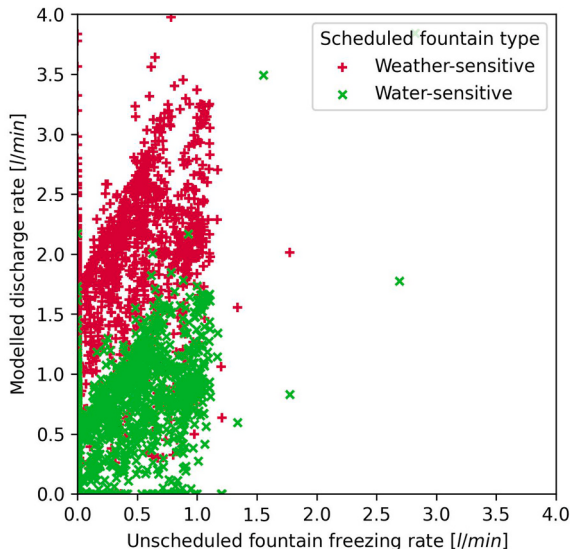


Fig. 8. Comparison of the freezing rate estimated for the non-scheduled fountain and the discharge rate of the scheduled fountains.

observed among the three kinds of fountains. The modelled weather- and water-sensitive discharge rate values were a factor of two and three smaller, respectively, than the measured non-scheduled discharge rate (Fig. 7b).

4.5. Pressure losses

Pressure consumption across the fountain pipeline provides insights into how it can be better optimized. The pipeline configuration of the automated ice stupa fountain is presented in Table 4. Pressure drops due to frictional losses across the length of the pipeline and due to the design of the fountain nozzle. Maximum frictional loss occurs during maximum discharge, which was measured to be $11\ l/min$. By substituting the corresponding values in Eq. 5, we get $P_{friction}$ to be $0.3\ bar$. The speed v can be determined from the discharge rate observation using Eq. 3. Therefore, from Eq. 4, P_F was estimated to be $4.6\ bar$, which represents more than 75% of the source water pressure. Most of the input pressure

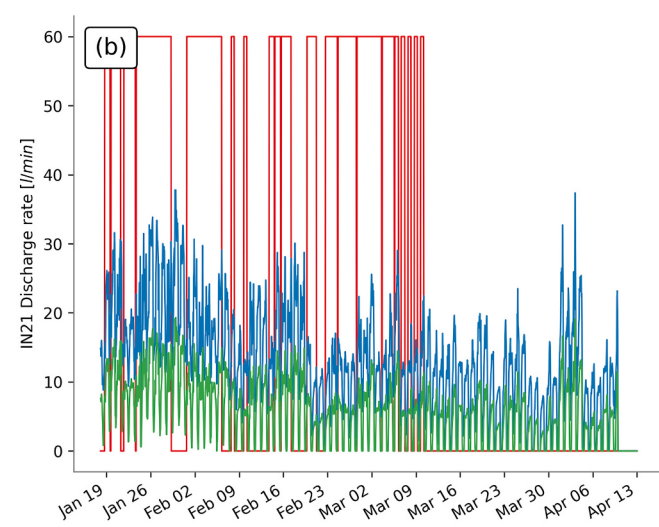


Table 4
Pipeline configuration of the automated ice stupa.

Name	Symbol	Value
Pipeline diameter	d_{ap}	16 mm
Pipeline length	L_p	66 m
Source water pressure	P_{source}	6 bar
Altitudinal pressure head	P_{alt}	1.1 bar
Water viscosity	μ	0.00152 Pas

was used by the fountain nozzle to generate water droplets.

4.6. Influence of wind-driven redistribution on fountain spray radius

The estimated volume changes during the month of January of the Swiss AIRs built in the winter of 2021–22 is less than half that of the AIRs from the previous winter (CH21). This difference cannot respond to warmer temperatures during the CH22 winter, as the median January temperature of CH22 winter was colder than that of the CH21 winter (Fig. 9a). Moreover, the volume growth of CH20 AIR is 6 times that of the CH22 AIR, despite CH22 winter being 3 C warmer.

We suspect the primary driver of volume difference across different winters to be the spray radius (Fig. 9b). However, this observation contradicts our expectation that AIRs using the same water source and fountain designs would present similar spray radius. Moreover, manual measurements of the fountain spray radius were lower than the drone observations of the ice radius. These two observations imply that wind drift of water droplets could play a major role in temporal fluctuations of ice radius.

To validate this hypothesis, the projectile motion of scheduled fountain water droplets were modelled with wind speed values taken from CH22 and CH21 experiments. Fig. 10 shows the modelled spray radius produced using these two wind datasets and compares them with the measured spray radius values. As illustrated, wind speed drives the temporal variation in the spray radius. Moreover, the spray radius of the scheduled fountain is much higher with CH22 wind values than with those of CH21. Therefore, the determination of the fountain spray radius cannot be performed using the characteristics of the fountain nozzle alone, as this is strongly influenced by the temporal variation of the wind speed.

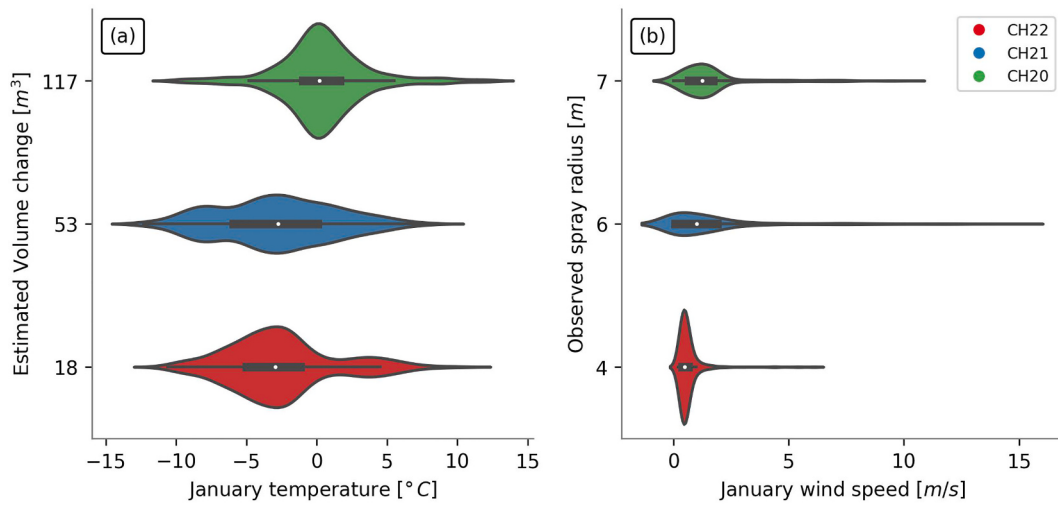


Fig. 9. (a) Estimated volume change and temperature. (b) Observed spray radius and wind speed during January for AIRs built across three winters.

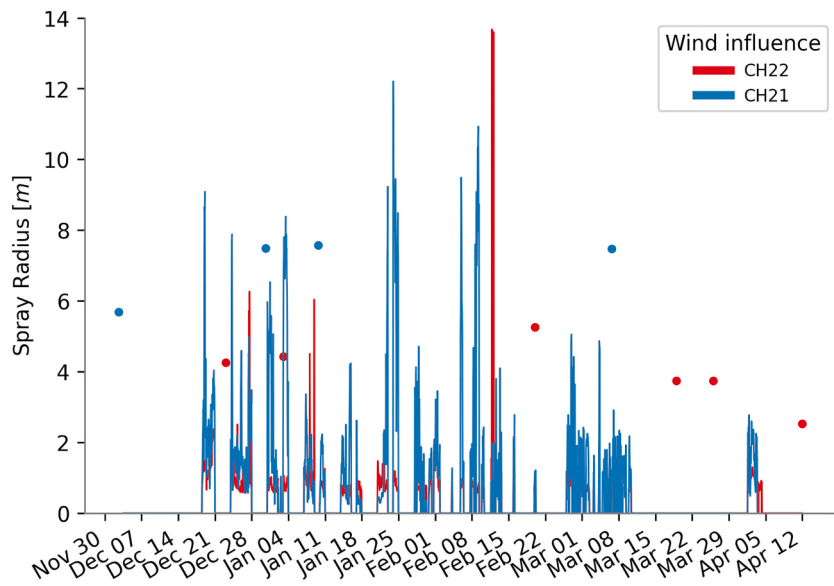


Fig. 10. Modelled spray radius using wind values from CH22 and CH21 experiments. Measured spray radius values are indicated as dots.

5. Discussion

5.1. Recommendations and challenges to improve AIR hardware tools

The present study shows one strategy that can improve the water-use efficiency of AIRs. We chose this strategy because it enables the use of the AIR model in a simple and effective manner. However, all these construction strategies are limited by the tools they use, namely the fountain, the pipeline and the automation system as described below:

5.1.1. Fountain optimisation

Contrary to the model assumptions, the parameters used to define the fountain were not independent. The fountain height, aperture diameter, discharge rate, water temperature and spray radius were related through the trajectories of the water droplets. The fountain nozzle design is crucial for increasing the ice volume obtained. It determines the diameter of the water droplets and the angle of launch for their projectile motion. The choice of these two parameters determines the rate of nucleation process, pressure losses and discharge rate ranges. For example, during the IN21 experiment, snow formation was

observed, indicating that the fountain water droplets have the potential to freeze before deposition on the AIR surface. In the CH22 experiment, the higher aperture diameter of the non-scheduled fountain nozzle (Fig. 2) produced bigger droplets and, therefore, had a lower fountain pressure loss when compared to the scheduled fountain. However, fountains with large aperture diameters lose their ability to form water droplets at low discharge rates. Therefore, the scheduled fountain nozzle design was used since it was able to produce water droplets with discharge rates as low as 2 l/min.

However, no methodology currently exists to rank the different fountain nozzles used for construction. Quantifying processes influenced by the fountain nozzle is challenging as it would require modelling the conduction, convection, wind redistribution, and nucleation processes that droplets of varying diameters undergo during their flight time. Instead, controlled experiments comparing the freezing rates between different fountain diameters have a better chance to yield insights on the engineering design of fountain nozzles.

5.1.2. Pipeline optimisation

An ideal pipeline configuration could make this technology cheaper

and maintenance free. However, optimization of the pipeline material and diameters is yet to be performed—despite the time lost on pipeline freezing events and the potential cost reduction with cheaper pipeline materials and sizes. Larger pipeline diameters reduce the occurrence of pipeline freezing events but increase the cost dramatically. In Ladakh, pipeline diameters used have a wide range (from 0.03 to 0.3 m) since the choice of pipeline diameter also depends on the additional insulation provided and whether or not it is buried. Therefore, a comprehensive cost-benefit analysis of different combinations of insulation and pipeline materials is required to determine the optimum design of the insulated pipeline system.

5.1.3. Cost reduction of automation system

Our strategy is not yet suitable for application in current AIR construction sites due to the cost of the automation system (around 8000 USD). However, we believe upto 10 fold cost reduction is possible through simpler automation systems which control only the duration of fountain spray and not their quantity.

5.2. New ways to upscale irrigation water supply

In this section, two hypothetical ice stupa construction scenarios namely, present and future are described. The present scenario is a depiction of the construction efforts based on oral interviews and field experience. The future scenario is a depiction of how the automation system developed can transform current construction efforts. The objective of both the scenarios is to maximize the meltwater available for irrigation. Both these scenarios are motivated by the construction campaigns conducted in the Ganges valley of Ladakh during the winter of 2019/20 ([Fig. 11](#)). This is the same valley where the IN21 study site was located enabling us to extrapolate some of the freezing rates and ice volume estimations from [Balasubramanian et al. \(2022\)](#). We conservatively assume that the valley had a total water supply of around 120 l/min, a winter duration of 4 months and the fountain was operational for only 8 h per day for both the scenarios.

5.2.1. Present scenario

In the present scenario, only two fountains could be operated

simultaneously using the available water supply. This limited the construction period of each ice stupa to just two months. Moreover, pipelines froze inside with ice blocks every few nights ([Fig. 7b](#)). This resulted in two farmers investing more than two months removing ice blocks and repairing the fountain pipeline system to make four ice stupas. Assuming each ice stupa had a maximum ice volume similar to IN21, we expect the total ice volumes frozen in this valley to be around 3 million litres.

5.2.2. Future scenario

In the future scenario, the automation system reduces the water consumption of each ice stupa by half. This enabled two farmers to build eight ice stupas spending less than a week of effort since there were no pipeline freezing events to deal with. The total ice volumes frozen, however, resulted in more than two times higher irrigation water supply from mid-April to mid-June.

6. Conclusions

An automated AIR construction strategy was compared with a manual one using data collected in Guttannen, Switzerland and Ganges, India.

The main purpose of the present study is to quantify the influence of different fountain scheduling strategies on the water-use efficiency and ice volume of AIRs exposed to identical weather conditions. It was found that overwatering by non-scheduled fountains not only increased the fountain spillwater production but also enhanced the melting rate of AIRs, mainly due to surface albedo and fountain heat flux feedbacks. Scheduled fountains, in contrast, consumed only 13% of the non-scheduled fountain water supply. However, volume evolution of both AIRs showed no significant variations.

Two different model forcing strategies were used to recommend two types of scheduled discharge rates: limited weather windows to favor higher ice volume and water supply to favor water-use efficiency. These model versions were able to capture more than 44% of the freezing rate variations of the manual AIR. Simulations converting non-scheduled fountains of Swiss and Indian locations to scheduled ones showed that at least a threefold increase in water-use efficiency is possible without compromising meltwater production.



Fig. 11. More than a month of effort from a dozen farmers were required to build five ice stupas across the Ganges valley in the winter of 2019/20. This research provides tools that two farmers can leverage to guarantee two times more winter water storage and reduce maintenance requirements to just a few days.

The influence of wind-driven redistribution on the spray radius resulted in AIRs six times larger, despite 3°C higher temperatures. This implies that higher wind speed caused the volume differences in the AIRs constructed at the Swiss location through three consecutive winters. Future selection of construction locations and design of automation algorithms need to capitalize on wind-driven redistribution effects to further increase water-use efficiency.

Fountain nozzles play an important role in the construction process. First, these consume most of the input water pressure to form water droplets. Second, their engineering design determines the droplet size distribution and spray radius. Future research, therefore, must be devoted to engineer fountain nozzles able to create water droplets with a size distribution that consumes less energy and a trajectory that increases the spray radius.

Funding

This work was supported and funded by the University of Fribourg and by the Swiss Government Excellence Scholarship (SB). The associated fieldwork in Guttannen was funded by the Glaciers Alive Association.

Declaration of Competing Interest

The authors declare that they have no known competing financial

interests or personal relationships that could have appeared to influence the work reported in this paper.

The authors declare the following financial interests/personal relationships which may be considered as potential competing interests:

Suryanarayanan Balasubramanian reports equipment, drugs, or supplies was provided by Glaciers Alive Association. Suryanarayanan Balasubramanian reports financial support and administrative support were provided by Swiss Government Excellence Scholarship.

Data availability

Data will be made available on request.

Acknowledgements

This work would not have been possible without the unconditional support of Daniel Bürgi from Guttannen Bewegt Association to manage our field experiments for the past three winters. David Sciboz, Maria Gruber and Dominik Amschwendt helped us to install the weather station and the automation system. The smooth operation of the automation system was possible due to the user interface designed by Martin Von Burg. We would particularly like to thank our english editors Ana Rodríguez Crespo and Akshatha N Tirumale. We also thank Dr. Eric Pohl for valuable suggestions that improved the manuscript.

Appendix A. Model forcing based on water-use efficiency and maximum ice volume objectives

To reduce model complexity and data requirement (Balasubramanian et al., 2022), assumptions that optimize ice volume (IVOM) or water-use efficiency (WEOM) were used. The freezing rate and melting rate were defined as the positive and negative mass change rate, respectively. The assumptions chosen were based on whether these overestimate or underestimate the freezing rate. IVOM assumptions overestimate freezing rate, whereas WEOM assumptions underestimate freezing rate. The application of these two kinds of assumptions on each energy balance component are described below.

A.1. Surface area A_{cone} assumptions

Determination of surface area during the accumulation period is achieved by assuming a constant ice cone radius equal to the fountain spray radius. The surface area scales the freezing rate of the AIR. Hence, for the IVOM version, the maximum possible slope was assumed to be 1 for the ice cone. Therefore, area is estimated as:

$$A_{cone} = \sqrt{2} \cdot \pi \cdot r_F^2 \quad (\text{A1})$$

Similarly, for the water-use efficiency objective, the area of the conical AIR is approximated to the area of its circular base. Therefore, area is estimated as:

$$A_{cone} = \pi \cdot r_F^2 \quad (\text{A2})$$

A.2. Net shortwave radiation q_{swLg} assumptions

The net shortwave radiation q_{sw} is computed as follows:

$$q_{sw} = (1 - \alpha) \cdot (SW_{direct} \cdot f_{cone} + SW_{diffuse}) \quad (\text{A3})$$

where α is the albedo value, SW_{direct} is the direct shortwave radiation, $SW_{diffuse}$ is the diffuse shortwave radiation, and f_{cone} is the solar area fraction.

The data requirement was reduced by estimating the global shortwave radiation and pressure using directly the location's coordinates and altitude through the solar radiation model described in Holmgren et al. (2018). The algorithm used to estimate the clear-sky global radiation is described in Ineichen (2008).

The diffuse and direct shortwave radiation are determined using the estimated global solar radiation as follows:

$$\begin{aligned} SW_{diffuse} &= cld \cdot SW_{global} \\ SW_{direct} &= (1 - cld) \cdot SW_{global} \end{aligned} \quad (\text{A4})$$

where cld is the cloudiness factor. cld is assumed to be 1 and 0 for the water-use efficiency and ice volume objective, respectively.

The variations in the albedo were ignored and it was assumed to be equal to snow albedo and ice albedo for the ice volume and water-use efficiency

objective, respectively.

The solar area fraction f_{cone} of the ice structure exposed to the direct shortwave radiation depends on the shape considered and is computed as:

$$f_{cone} = \frac{(0.5 \cdot r_{cone} \cdot h_{cone}) \cdot \cos\theta_{sun} + (\pi \cdot (r_{cone})^2 / 2) \cdot \sin\theta_{sun}}{\pi \cdot r_{cone} \cdot ((r_{cone})^2 + (h_{cone})^2)^{1/2}} \quad (A5)$$

For the ice volume objective, the slope of the cone was assumed to be 1; f_{cone} is determined as follows:

$$f_{cone} = \frac{\cos\theta_{sun} + \pi \cdot \sin\theta_{sun}}{2\sqrt{2} \cdot \pi} \quad (A6)$$

Similarly, for the water-use efficiency objective, the slope of the cone was assumed to be negligible.

$$f_{cone} = \frac{\sin\theta_{sun}}{2} \quad (A7)$$

A.3. Net longwave radiation $q_{LW}Lg$ assumptions

To determine outgoing longwave radiation, $T_{ice} = 0^\circ C$ was assumed. To constrain the minimum ice temperature is challenging; therefore, this assumption was maintained for both our objectives. However, to estimate atmospheric emissivity, cld was assumed to be 1 and 0 for the water-use efficiency and ice volume objective, respectively.

A.4. Turbulent fluxes assumptions

Turbulent fluxes estimation depends on the slope of the cone through the μ_{cone} parameter. As suggested by Oerlemans et al. (2021), this parameter was estimated as follows:

$$\mu_{cone} = 1 + s_{cone}/2 \quad (A8)$$

Hence, the μ_{cone} parameter takes values of 1.5 and 1 for the ice volume and water-use efficiency objective, respectively. Since turbulent fluxes impact both the freezing and the melting rates, this assumption may not favor the corresponding objectives for certain sites.

Table A1. Parameters in the model categorized as constant, model hyperparameters, and weather parameters with their respective values/ranges.

Constant parameters	Symbol	Value	Unit	References
Van Karman constant	κ	0.4	dimensionless	Cuffey and Paterson (2010)
Stefan Boltzmann constant	σ	5.67×10^{-8}	$Wm^{-2}K^{-4}$	Cuffey and Paterson (2010)
Air pressure at sea level	p_0, a	1013	hPa	Mölg and Hardy (2004)
Density of water	ρ_w	1000	kgm^{-3}	Cuffey and Paterson (2010)
Density of ice	ρ_{ice}	917	kgm^{-3}	Cuffey and Paterson (2010)
Density of air	ρ_a	1.29	kgm^{-3}	Mölg and Hardy (2004)
Specific heat of water	c_w	4186	$Jkg^{-1}C^{-1}$	Cuffey and Paterson (2010)
Specific heat of ice	c_{ice}	2097	$Jkg^{-1}C^{-1}$	Cuffey and Paterson (2010)
Specific heat of air	c_a	1010	$Jkg^{-1}C^{-1}$	Mölg and Hardy (2004)
Thermal conductivity of ice	k_{ice}	2.123	$Wm^{-1}K^{-1}$	Bonales et al. (2017)
Latent heat of sublimation	L_s	2.848×10^6	Jkg^{-1}	Cuffey and Paterson (2010)
Latent heat of fusion	L_f	3.34×10^5	Jkg^{-1}	Cuffey and Paterson (2010)
Gravitational acceleration	g	9.81	$m s^{-2}$	Cuffey and Paterson (2010)
Weather station height	h_{AWS}	2	m	assumed
Model timestep	Δt	3600	s	assumed
Uncertain parameters	Symbol	Range	Unit	References
Surface layer thickness	Δx	[0.01, 0.10]	m	assumed
Ice emissivity	ϵ_{ice}	[0.95, 0.99]	dimensionless	Hori et al. (2006)
Surface roughness	z_0	[0.001, 0.005]	m	Brock et al. (2006)
Ice albedo	α_{ice}	[0.15, 0.35]	dimensionless	Steiner et al. (2015); Zolles et al. (2019)
Snow albedo	α_{snow}	[0.8, 0.9]	dimensionless	Zolles et al. (2019)
Precipitation temperature threshold	T_{ppt}	[0, 2]	°C	ShiChang et al. (2010)
Albedo decay rate	τ	[10, 22]	days	Schmidt et al. (2017); Oerlemans and Knap (1998)

References

- Aggarwal, A., Frey, H., McDowell, G., Drenkhahn, F., Nüsser, M., Racoviteanu, A., Hoelzle, M., 2021. Adaptation to climate change induced water stress in Major Glacierized Mountain Regions. *Clim. Dev.* 0, 1–13. <https://doi.org/10.1080/17565529.2021.1971059>.
- Awaz Production, 2022. Ice Stupa|Artificial Glacier Grafting in Skardu. <https://youtu.be/iMDN0H0tnQg>.
- Balasubramanian, S., Hoelzle, M., Lehning, M., Bolibar, J., Wangchuk, S., Oerlemans, J., Keller, F., 2022. Influence of meteorological conditions on artificial Ice Reservoir (Icestupa) evolution. *Front. Earth Sci.* 9 <https://doi.org/10.3389/feart.2021.771342>, 771–342.
- Batchelor, G., 2000. An Introduction to Fluid Dynamics. Cambridge Mathematical Library, Cambridge University Press. URL. <https://books.google.fr/books?id=Rla7OihRvUgC>.
- BBC News, 2020. Bright Artificial Glacier in Naryn - BBC Kyrgyz. <https://www.youtube.com/watch?v=TpeSQf75bfQ>.
- Bonales, L.J., Rodriguez, A.C., Sanz, P.D., 2017. Thermal Conductivity of Ice prepared under Different Conditions. *Int. J. Food Prop.* 20, 610–619. <https://doi.org/10.1080/10942912.2017.1306551>.
- Brock, B.W., Willis, I.C., Sharp, M.J., 2006. Measurement and parameterization of aerodynamic roughness length variations at Haut Glacier d’Arolla, Switzerland. *J. Glaciol.* 52, 281–297. <https://doi.org/10.3189/172756506781828746>.

- Clouse, C., Anderson, N., Shippling, T., 2017. Ladakh's artificial glaciers: climate-adaptive design for water scarcity. *Clim. Dev.* 9, 428–438. <https://doi.org/10.1080/17565529.2016.1167664>.
- Cuffey, K., Paterson, W., 2010. The Physics of Glaciers. Elsevier Science. URL: <https://books.google.fr/books?id=Jca2v1u1EKEC>.
- Hersbach, H., Bell, B., Berrisford, P., Hirahara, S., Horányi, A., Muñoz-Sabater, J., Nicolas, J., Peubey, C., Radu, R., Schepers, D., Simmons, A., Soci, C., Abdalla, S., Abellán, X., Balsamo, G., Bechtold, P., Biavati, G., Bidlot, J., Bonavita, M., Chiara, G., Dahlgren, P., Dee, D., Diamantakis, M., Dragani, R., Flemming, J., Forbes, R., Fuentes, M., Geer, A., Haimberger, L., Healy, S., Hogan, R.J., Hólm, E., Janisková, M., Keeley, S., Laloyaux, P., Lopez, P., Lupu, C., Radnoti, G., de Rosnay, P., Rozum, I., Vamborg, F., Villaume, S., Thépaut, J.-N., 2020. The ERA5 global reanalysis. *Q. J. R. Meteorol. Soc.* 146, 1999–2049. <https://doi.org/10.1002/qj.3803>.
- Holmgren, W.F., Hansen, C.W., Mikofski, M.A., 2018. Pvlib python: a python package for modeling solar energy systems. *J. Open Source Softw.* 3, 884. <https://doi.org/10.21105/joss.00884>.
- Hori, M., Aoki, T., Tanikawa, T., Motoyoshi, H., Hachikubo, A., Sugiura, K., Yasunari, T. J., Eide, H., Storvold, R., Nakajima, Y., Takahashi, F., 2006. In-situ measured spectral directional emissivity of snow and ice in the 8–14 μm atmospheric window. *Remote Sens. Environ.* 100, 486–502. <https://doi.org/10.1016/j.rse.2005.11.001>.
- Immerzeel, W.W., Lutz, A.F., Andrade, M., Bahl, A., Biemans, H., Bolch, T., Hyde, S., Brumby, S., Davies, B.J., Elmore, A.C., Emmet, A., Feng, M., Fernández, A., Haritashya, U., Kargel, J.S., Koppes, M., Kraaijenbrink, P.D.A., Kulkarni, A.V., Mayewski, P.A., Nepal, S., Pacheco, P., Painter, T.H., Pellicciotti, F., Rajaram, H., Rupper, S., Sinisalo, A., Shrestha, A.B., Viviroli, D., Wada, Y., Xiao, C., Yao, T., Baillie, J.E.M., 2020. Importance and vulnerability of the world's water towers. *Nature* 577, 364–369. <https://doi.org/10.1038/s41586-019-1822-y>.
- Ineichen, P., 2008. A broadband simplified version of the solis clear sky model. *Sol. Energy* 82, 758–762. <https://doi.org/10.1016/j.solener.2008.02.009>.
- IPCC, 2019. Chapter 2: High Mountain Areas — Special Report on the Ocean and Cryosphere in a Changing Climate, IPCC Special Report on the Ocean and Cryosphere in a Changing Climate. <https://doi.org/10.1017/9781009157964.004>.
- IPCC, 2022. Cross-Chapter Paper 5: Mountains, Climate Change 2022: Impacts, Adaptation and Vulnerability. Contribution of Working Group II to the Sixth Assessment Report of the Intergovernmental Panel on Climate Change. <https://doi.org/10.1017/9781009325844.022>.
- Meteoblue, 2021. Climate Guttannen. https://www.meteoblue.com/en/weather/historyclimate/climatemodelled/guttannen_switzerland_2660433.
- Mölg, T., Hardy, D.R., 2004. Ablation and associated energy balance of a horizontal glacier surface on Kilimanjaro. *J. Geophys. Res.-Atmos.* 109, 1–13. <https://doi.org/10.1029/2003JD004338>.
- Mukhopadhyay, B., Khan, A., 2015. A reevaluation of the snowmelt and Glacial melt in river flows within Upper Indus Basin and its significance in a changing climate. *J. Hydrol.* 527 <https://doi.org/10.1016/j.jhydrol.2015.04.045>.
- Nüsser, M., Baghel, R., 2016. Local Knowledge and Global Concerns: Artificial Glaciers as a Focus of Environmental Knowledge and Development Interventions. In: Meusburger, P., Freytag, T., Suarsana, L. (Eds.), Ethnic and Cultural Dimensions of Knowledge and Space. Springer International Publishing, Cham, pp. 191–209. https://doi.org/10.1007/978-3-319-21900-4_9.
- Nüsser, M., Dame, J., Kraus, B., Baghel, R., Schmidt, S., 2019a. Socio-Hydrology of artificial Glaciers in Ladakh, India: assessing adaptive strategies in a changing cryosphere. *Reg. Environ. Chang.* <https://doi.org/10.1007/s10113-018-1372-0>.
- Nüsser, M., Dame, J., Parveen, S., Kraus, B., Baghel, R., and Schmidt, S.: Cryosphere-fed irrigation networks in the northwestern Himalaya: precarious livelihoods and adaptation strategies under the impact of climate change, *Mt. Res. Dev.*, 39, doi: <https://doi.org/10.1659/MRD-JOURNAL-D-18-00072.1>, 2019b.
- Oerlemans, J., Knap, W.H., 1998. A 1 year record of global radiation and albedo in the ablation zone of Morteratschgletscher, Switzerland. *J. Glaciol.* 44, 231–238. <https://doi.org/10.3189/S0022143000002574>.
- Oerlemans, J., Balasubramanian, S., Clavuot, C., Keller, F., 2021. Brief Communication: growth and Decay of an Ice Stupa in Alpine Conditions – a simple Model Driven by Energy-Flux Observations over a Glacier Surface. *Cryosphere* 15, 3007–3012. <https://doi.org/10.5194/tc-15-3007-2021>.
- Palmer, L., 2022. Storing Frozen Water to Adapt to climate Change. *Nat. Clim. Chang.* 12, 115–117. <https://doi.org/10.1038/s41558-021-01260-x>.
- Reuters, 2021. Conservationists in Chile Aim to Freeze Water in Man-Made Glaciers. [Reuters](#).
- Schmidt, L.S., Ádalgeirs Ódóttir, G., Guðmundsson, S., Langen, P.L., Pálsson, F., Mottram, R., Gascoin, S., Björnsson, H., 2017. The Importance of Accurate Glacier Albedo for estimates of Surface Mass Balance on Vatnajökull: evaluating the Surface Energy Budget in a Regional climate Model with Automatic Weather Station Observations. *Cryosphere* 11, 1665–1684. <https://doi.org/10.5194/tc-11-1665-2017>.
- ShiChang, TanGuang, ShiQiao, G., Kang, Z.G.Z., 2010. Response of Zhadang Glacier Runoff in Nam Co Basin, Tibet, to changes in air temperature and precipitation form. *Chin. Sci. Bull.* 55, 2103–2110. <https://doi.org/10.1007/s11434-010-3290-5>.
- Steiner, J.F., Pellicciotti, F., Burl, P., Miles, E.S., W.T. D. I. W., 2015. Reid: modelling ice-cliff backwasting on a debris-covered glacier in the Nepalese Himalaya. *J. Glaciol.* 61, 889–907. <https://doi.org/10.3189/2015JoG14J194>.
- Vince, G., 2009. Glacier Man. *Science* 326, 659–661. <https://doi.org/10.1126/science.326.659>.
- Wangchuk, S., 2020. Ice Stupa Competition. <https://tribal.nic.in/IceStupa.aspx>.
- Zolles, T., Maussion, F., Galos, S.P., Gurgiser, W., Nicholson, L., 2019. Robust uncertainty assessment of the spatio-temporal transferability of Glacier mass and energy balance models. *Cryosphere* 13, 469–489. <https://doi.org/10.5194/tc-13-469-2019>.